metals

Article

Buckling of Bisegment Pressure Hulls Fabricated through Free Bulging

Yun Teng, Jian Zhang* and Feng Wang

School of Mechanical Engineering, Jiangsu University of Science and Technology, Zhenjiang 212003, China; tengyun730@stu.just.edu.cn (Y.T.); 199020074@stu.just.edu.cn (F.W.)
* Correspondence: zhjian127@just.edu.cn

Abstract: This study explored the buckling performance of bi-segment pressure hulls under external pressure. We fabricated bi-segment pressure hulls from bi-segment cylindrical preforms by using free bulging. The cylindrical preforms had a nominal thickness of 0.95 mm, nominal radius of 51 mm, and nominal height of 242 mm. Six bi-segment pressure hulls were hydrostatically and externally pressurised into buckling. Experimental results revealed that the maximum buckling load of the bi-segment pressure hulls was increased by 36.75% compared with that of the bi-segment cylinders. In addition, we performed a nonlinear finite element analysis to determine the bulging and buckling modes of the hulls. We noted that the nonlinear analysis results exhibited good agreement with the experimental data.

Keywords: bi-segment pressure hull; cylindrical preform; free bulging; buckling; external pressure

Citation: Teng, Y.; Zhang, J.; Wang, F. Buckling of Bisegment Pressure Hulls Fabricated through Free Bulging. *Metals* **2023**, *13*, 576. https://doi.org/10.3390/met13030576

Academic Editor: Vincenzo Crupi

Received: 14 February 2023
Revised: 28 February 2023
Accepted: 9 March 2023
Published: 13 March 2023

1. Introduction

Deep-sea space stations and autonomous underwater vehicles are crucial deep-sea exploration systems. The core components of these systems comprise multi-segment pressure hulls. Geometrically, these systems typically contain components such as multi-segment balls [1], multi-segment cones [2], and multi-segment barrels [3]. Multi-segment pressure shells offer many advantages, such as easy space expansibility, excellent buoyancy, and high buckling strength. However, in addition to their fabrication, the buckling of multi-segment shells remains a challenge.

Researchers have extensively studied the buckling performance of single barrels. For example, Błachut and colleagues have comprehensively analysed the elastic–plastic buckling of uniformly thick-walled barrels and the influences of geometry, material, and geometric imperfections on such buckling. Their results revealed that axisymmetric shells were particularly effective in increasing the static critical buckling load of the shells [4–9]. Jam and Kiani have studied the linear buckling analysis of nanocomposite conical shells reinforced with single-walled carbon nanotubes. The results showed that their volume and distribution had significant effect on the buckling pressure and circumferential [10]. Similarly, different kinds of shells based on functionally graded graphene have been analysed [11,12], and it is found that graphene could strengthen the buckling behaviour and stress. Jasion and colleagues have intensively investigated the effect of geometry on the strength and elastic stability of barrelled shells. They analytically described the problem of barrelled shell buckling. Their analyses involved assumptions that the shells were isotropic, homogeneous and of constant thickness. They thus applied the Bubnov–Galerkin method to determine the buckling state. Furthermore, they presented numerical examples of barrelled shells for linear eigenvalue buckling prediction and nonlinear post-buckling analysis. Their analytical and numerical results exhibited good agreement. In addition, they discussed the advantages of barrelled shells over cylindrical shells and argued that barrelled shells with a positive Gaussian curvature have a higher critical buckling load [13–15]. Zhang and colleagues used 333 goose eggs to establish mathematical equations for describing the geometrical distribution, surface area, volume, and aspect ratio of the eggs. On the basis of their analysis results, they numerically and experimentally studied the buckling of bionic egg-shaped shells with uniform and nonuniform thicknesses [16–21].

Furthermore, researchers have extensively studied the buckling performance of multi-segment pressure shells. For example, Błachut and Smith investigated the buckling performance of multi-segment cylindrical shells under uniform hydrostatic pressure. They discussed the components of a multi-segment cylindrical shell structure with flanges and the shell structure without flanges. Moreover, they fabricated five samples using computerized numerical control (CNC) technology, tested them under external hydrostatic pressure and adopted numerical simulations that were compared with experimental results. The results exhibited a good agreement [3]. Zhang and Tang studied the buckling of bi-segment spherical shells with rib rings of different sizes. Specifically, they executed numerical and experimental analyses on the buckling of these shells. Their results revealed that shell instability is mainly governed by the stress distribution and geometry, and their numerical and experimental results showed a good agreement [22]. Zhang and Di studied the buckling behaviours of segmented toroids under external pressure. With the help of tungsten inert gas welding (TIG), they fabricated two segmented toroids and two continuous toroids. They performed buckling tests in a pressure chamber after all the toroids were manufactured. Subsequently, they analysed the linear buckling, nonlinear buckling, and imperfect sensitivity of the segmented toroids by performing finite element method (FEM) using the commercial software ABAQUS. Their results revealed good agreement between the numerical estimates and experimental observations [23]. Accordingly, they also investigated the influences of joint angle and segmented ring on the buckling of the segmented toroids under uniform external pressure. Their results indicated that joint angle had practically no influence on the buckling load of 0° and 180° non-segmented toroids, and the segmented ring significantly improved the buckling load of the 180° segmented toroids [24]. These shells were fabricated through CNC machining, cold pressing, or rapid prototyping techniques. However, these techniques have the following disadvantages, such as high manufacturing costs, long lead times, and high complexity.

In contrast to CNC machining, free bulging is a robust, economic, and flexible manufacturing method. The basic principle of free bulging is to fill a closed single-curvature shell with liquid medium and then pressurize until the target geometry is obtained. Free bulging can be used to manufacture large pressure vessels without dies. Its typical land-based applications include water containers, hydraulic tanks, and landmarks [25–28], and its typical underwater applications include single barrel shells [29,30] and single egg-shaped shells [31,32]. Nevertheless, studies on its land and underwater applications have been limited to single shells. No studies have been conducted on the buckling of multi-segment shells fabricated in the form of free bulging.

In this research, the buckling performances of bi-segment pressure hulls fabricated through free bulging were investigated. In general, the structure of a bi-segment pressure hull was put forward, providing geometrical and material definitions. In addition, on the one hand, the geometric parameters of the hoop rib at the shell intersection were determined in the case of the deformation consistency based on the provided data. On the other hand, the corresponding experiment was carried out, including fabricated six bi-segment cylindrical preforms, internally bulging, and externally collapsed. For verifying the experimental results, the effects of various bulging magnitudes were numerically explored by using the linear and nonlinear finite element method. The results indicated that nonlinear analysis results exhibited good agreements with the experimental data. The maximum improvement of the buckling strength of bi-segment hulls after free bulging was 36.75%.

2. Experimental Analysis

This section discusses the experimental flowchart, geometric measurement, and internal pressure tests of six bi-segment cylindrical preforms. Geometric measurements and external pressure tests of the bi-segment pressure hulls were performed at Jiangsu Provincial Key Laboratory of Advanced Manufacturing for Marine Mechanical Equipment, Jiangsu University of Science and Technology, China.

2.1. Material and Methods

2.1.1. Problem Statement

Six stainless steel bi-segment cylindrical preforms were fabricated, each internally rib-reinforced in the middle. One of the preforms was kept as reference and five others were bowed out by applying internal pressure to various degree of barrelling. All six were eventually collapsed by quasi-static external pressure. For each bi-segment cylindrical preform, L represents the total length, D represents the diameter, T represents the thickness, and H represents a single tube length, as presented in Figure 1. Both the steel plates and the hoop rib had the same diameter as the preform.

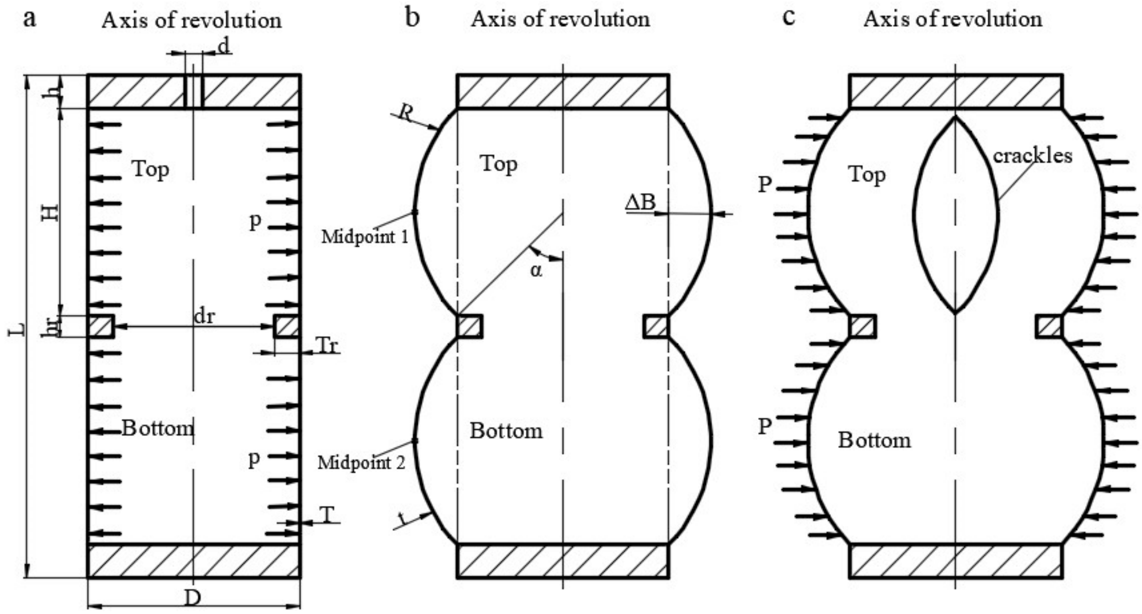

Figure 1. Schematic of a bi-segment cylindrical preform (**a**), bulged hull (**b**), and collapsed hull (**c**).

For each bi-segment cylindrical preform, the optimal thickness of the hoop rib could be found. In general, if the meridian of the bi-segment pressure hull has not exceeded a spherical shape, then the shell and hoop are displaced uniformly under external pressure. Namely, according to the deformation consistency of a spherical structure, it was assumed that the radial displacement hoop rib (δ_r) and the radial displacement of the whole spherical shell (δ_s) subjected to hydrostatic pressure were the same; they could be expressed as:

$$\delta_r = \frac{P_R D_r}{2E}\left(\frac{D_r^2 + d_r^2}{D_r^2 - d_r^2} - \mu\right), \tag{1}$$

$$\delta_s = \frac{PR^2 \sin\alpha}{2Et}(1-\mu), \tag{2}$$

$$\delta_s = \delta_r, \tag{3}$$

where P_R is the uniformly distributed external pressure,D_r and d_r are the outer diameter and inner diameter of hoop rib, respectively, μ is the Poisson's ratio of the material, t is the thickness of the spherical shell, R is the radius of the spherical shell, and α is the intersection angle [22,24,33,34].

There are two parameters, P_R and d_r, in the above equation, and based on geometric as well as mechanical relationships, they could be deduced as:

$$d_r = D_r - 2T_r, \tag{4}$$

$$P_R = P + \frac{2F\cos a}{h_r}, \tag{5}$$

where P is operation pressure, F is linear stress along the edge of the hoop ring, h_r is the length of the hoop rib, T_r is the thickness of the hoop rib.

Next, the thickness of the hoop rib can be derived using Equation (6). Table 1 lists the nominal dimensions of the cylinder, plates, and hoop rib. Table 2 lists the nominal dimensions of the bulged hull.

$$T_r = \frac{D_r}{2}\left[1 - \sqrt{\frac{R^2\sin\alpha(1-\mu)h_r + (\mu-1)(R\cos\alpha + h_r)D_r t}{R^2\sin\alpha(1-\mu)h_r + (\mu+1)(R\cos\alpha + h_r)D_r t}}\right]. \tag{6}$$

Table 1. Nominal dimensions of bi-segment cylindrical preform, plate, and hoop rib.

Parameters	Values/mm
Tube Outer Diameter (D)	102
Tube Length (H)	100
Plate Diameter (D)	102
Plate Length (h)	16
Hoop Rib Inner Diameter (dr)	78
Hoop Rib Thickness (Tr)	12
Hoop Rib Length (hr)	10
Total Length (L)	242

Table 2. Nominal dimensions of bulged hull.

Parameters	Values
Intersection angle (α)	45 (°)
Radius of spherical shell (R)	72.5 (mm)
Thickness of spherical shell (t)	0.58 (mm)

In addition, a general water valve was integrated into the top plate to facilitate the execution of free bulging. After each preform was subjected to free bulging, the water inside was removed, the water valve was closed using a hex screw, and the bi-segment pressure hull buckled under external pressure. The material properties were determined by subjecting three stainless-steel coupons to a uniaxial tensile test. The test process was previously reported by our team [29]. The test results revealed a bilinear stress versus strain relationship, as displayed in Figure 2. Accordingly, the following bilinear elastic–plastic mechanics equation was used to determine the material constitutive relationships. Table 3 lists the material properties determined from the uniaxial tensile test.

$$\begin{cases} \sigma_{eq} = E_1\varepsilon_{eq}, & \sigma_{eq} < \sigma_y \\ \sigma_{eq} = \sigma_y + E_1\varepsilon_{eq}, & \sigma_{eq} > \sigma_y \end{cases} \tag{7}$$

where Young's modulus E can be determined from the slope of the first linear segment, Poisson's ratio μ can be determined from the ratio of transverse to longitudinal strains, the yield point σ_y can be determined from the proof stress (defined as 0.2% herein), and the strength coefficient E_1 can be determined from the slope of the second linear segment.

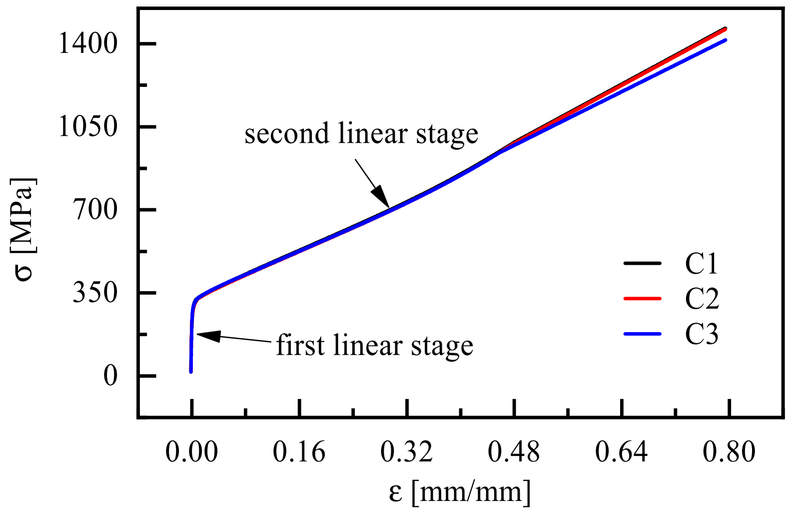

Figure 2. True stress–strain curves of parent material obtained from a uniaxial tensile test [29].

Table 3. Material properties determined from uniaxial tensile test [29].

Coupon	σ_y/MPa	E_1/GPa	E/GPa	μ
C1	288.5	1310.6	214.4	0.27
C2	286.2	1307.2	208.1	0.28
C3	279.1	1298.1	195.5	0.29
AVE	284.6	1305.3	206.0	0.28

2.1.2. Measuring and Testing

As mentioned, six bi-segment cylindrical preforms were fabricated, subjected to free bulging, and tested (Figure 1). The experimental methodology adopted in this study involved eight steps (Figure 3): (a) fabrication of cylindrical preforms, (b) shape measurement of cylindrical preforms, (c) thickness measurement of cylindrical preforms, (d) free bulging of segment hulls, (e) thickness measurement of segment hulls, (f) shape measurement of segment hulls, (g) hydrostatic testing of segment hulls, and (h) observation of buckling modes of segment hulls.

The external geometry of each cylindrical preform was measured optically before and after bulging by using an industrial-grade three-dimensional (3D) scanner (Cronos X, Open Technologies Inc., Brescia, Italy). The corresponding software was Optical RevEng (Optical RE v2.3, Open Technologies Inc., Brescia, Italy). Before the scanning process, the outer surface of each sample was uniformly sprayed with a type FC-5 intensifying contrast agent (Hyperd NDT-Material, Shanghai Yue Ci Electronic Technology Inc., Shanghai, China), which significantly improved the scanning performance. The scanning process was performed using Optical RevEng software with a scanning accuracy of <0.02 mm; smooth meshes were used for the slices. After the scanning process, all slices were stitched together to produce a digital sample.

The thickness of each cylindrical preform was measured before and after bulging by using an ultrasonic micrometer (PX-7, Dakota Ultrasonics Inc., Scotts Valley, CA, USA) with an accuracy of <0.002 mm. During the measurement process, a low-viscosity coupling reagent (100 ML, Elecall Electric Inc., Yueqing, China) was used to smooth the surface of the measurement sample and facilitate its reading. For each preform, thickness measurements were performed at 352 evenly distributed points (16 axial points × 22 circumferential points). To determine the variation in the thickness of the bulged preform, the same measurement points were used for the bulged hulls.

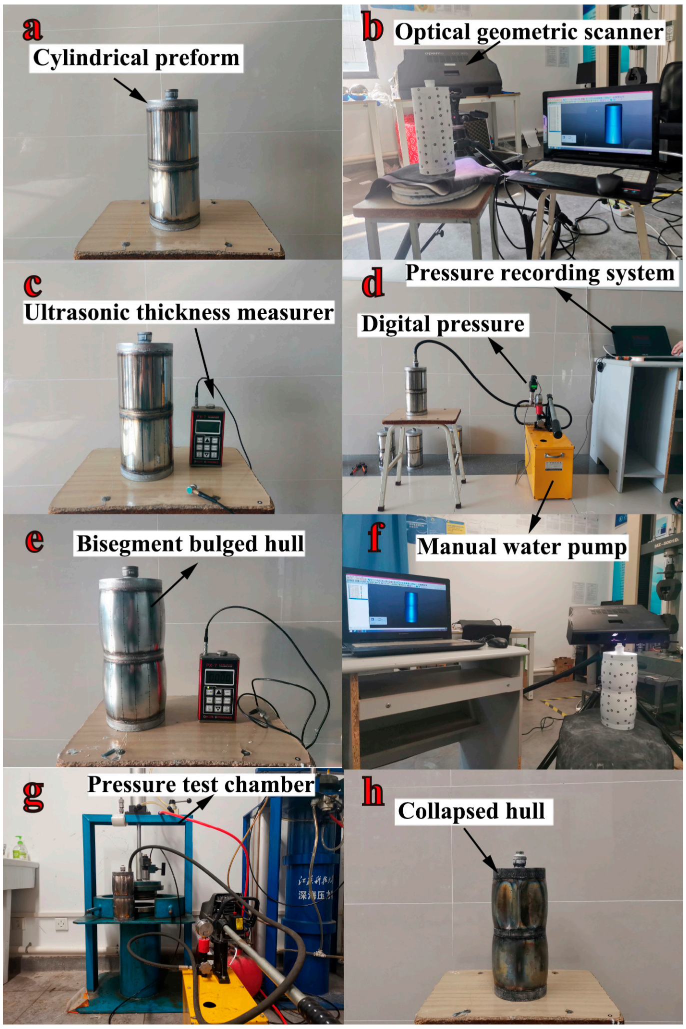

Figure 3. Experimental procedure for buckling of free-bulged bi-segment pressure hulls under external pressure.

Notably, one of the six preforms (designated as preform 1) was considered a special case and was used as a reference. The bulging magnitude for this preform was zero, and the preform was directly tested to collapse under external pressure instead. The remaining five preforms (preforms 2–6) were internally bulged under different magnitudes and then externally collapsed to destruction. The test field and instruments were located at Jiangsu Provincial Key Laboratory of Advanced Manufacturing for Marine Mechanical Equipment, Jiangsu University of Science and Technology, China. Before the internal free bulging test, each preform sample was subjected to a load of 1 MPa and then maintained for 60 s to assess the sealing quality of the weld. This load is lower than the plastic bulging pressure (6.12 MPa) of a cylinder, and the bulging pressure can be derived as follows [29]:

$$p = \frac{2}{\sqrt{3}} \frac{\sigma_y T}{R}, \quad (8)$$

where T is the thickness of the preform and k is the material volume coefficient, which can be expressed as follows:

$$k = 2.79154E - 06\Delta B^3 - 2.92802E - 04\Delta B^2 - 1.39745E - 04\Delta B + 1 \quad (9)$$

In the free bulging test, each preform was filled with tap water by using a manual water pump (SY-300X, Zhenhuan Hydraulic Equipment Factory, Taizhou, China), and the bulging load was recorded by a digital pressure sensor. Next, the unloading spout of the manual water pump was slowly opened to release the bulging pressure inside the hull, and the remaining tap water inside the hull was poured through the filling spout. Subsequently, the bulged hull was transferred into a pressure test chamber, where a manual pump applied pressure and a digital pressure sensor recorded the pressure values. The maximum pressure recorded for each bi-segment pressure hull corresponded to its critical buckling load. As the pressure increased, the bi-segment pressure hull was buckled with a loud noise. Finally, the chamber pressure was released, followed by the removal of the buckled hulls so that the destruction mechanism of each free-bulged hull could be observed. The pressure test chamber was developed by our team and placed at Jiangsu Provincial Key Laboratory of Advanced Manufacturing for Marine Mechanical Equipment, Jiangsu University of Science and Technology. It has an internal diameter of 200 mm, a height of 400 mm, and a maximum working pressure of 10 MPa. For the aforementioned free bulging and external buckling tests, the same digital pressure sensor (SUP-P3000, range: 0–20 MPa, measurement accuracy: <0.01 MPa), pressure acquisition device (both from Donghua Test Technology Inc., Shanghai, China), hydraulic medium, and manual water pump were adopted.

2.2. Experimental Results and Discussion

2.2.1. Measuring Analysis

The geometry measurement results for the bi-segment cylindrical preforms indicated reasonable repeatability and fabrication accuracy. As illustrated in Figure 4, the six bi-segment cylindrical preforms fabricated in this study deviated slightly from the perfect geometries. The deviations were mainly located near the welds of the hoop rib and the two thick plates. This can be attributed to welding deformations and uneven welds. The maximum shape deviation of the six preforms ranged from 0.53 to 1.31 mm. However, for each preform, the remaining areas without the welds exhibited fairly high accuracy. The corresponding shape deviations were mainly within ±0.4 mm.

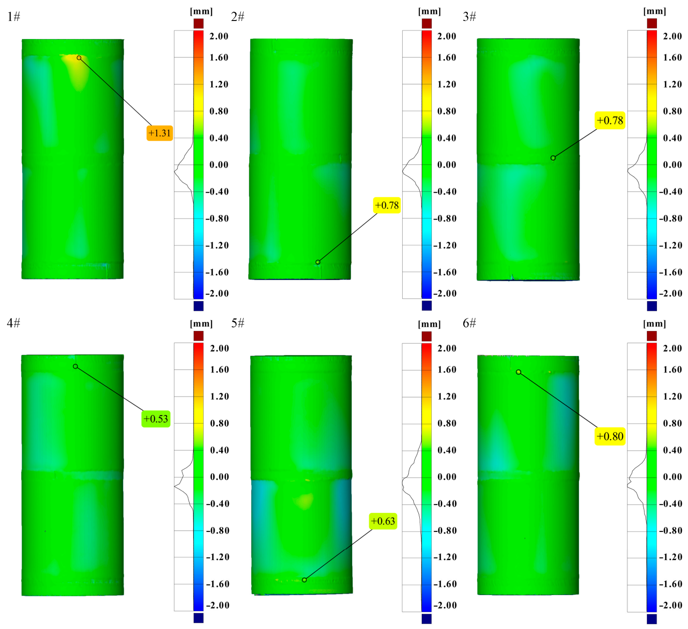

Figure 4. Shape deviations from the perfect geometry for six fabricated bi-segment cylindrical preforms.

The bi-segment pressure hulls subjected to free bulging were symmetrical about the axis of rotation, and their deformation symmetry increased with the bulging magnitude. As presented in Figure 5, the geometries of the bi-segment pressure hulls deviated significantly from perfect geometries due to the slightly nonuniform thickness of the hulls before bulging and initial geometric imperfections. Figure 6 displays the shape deviations between the bi-segment cylindrical preforms and the corresponding hulls subjected to free bulging. The bulged hulls exhibited reasonable symmetry (Figures 5 and 6). The maximum deformation occurred at the midpoint of the top or bottom shell of the bi-segment pressure hulls, and this was attributed to the initial geometric imperfections and to the nonuniform thickness distribution. Bulging magnitudes ΔB that were applied to the bi-segment cylindrical preforms tested in this study are listed in Tables 3 and 4. The height growth rate of the bi-segment pressure hulls essentially remained constant as the bulging magnitude increased. These results are consistent with those of previous studies on the buckling properties of bulged barrels under external pressure [30].

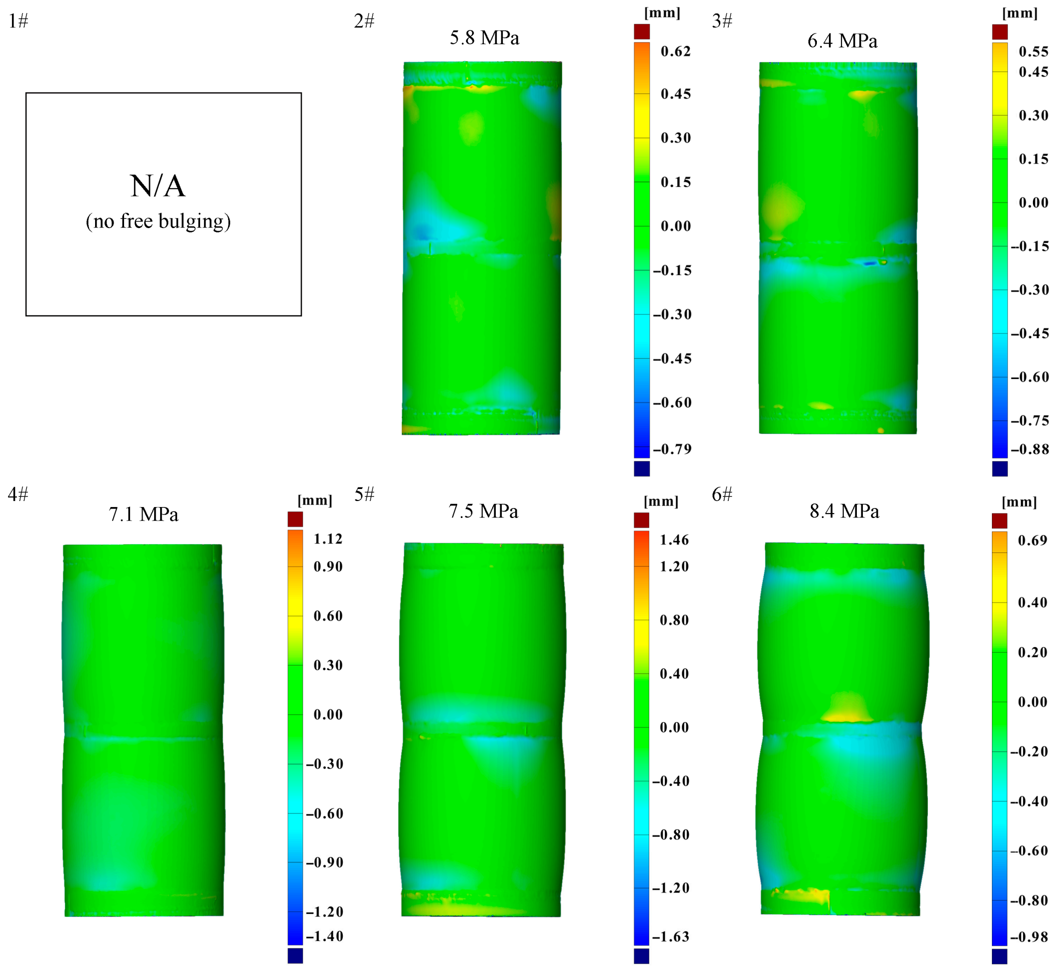

Figure 5. Shape deviations from the perfect geometry for bi-segment bulged hulls.

The thickness of each preform was evenly distributed and exhibited favourable repeatability. The wall thicknesses of the top and bottom shells of each preform is presented in Table 5 and Figure 7. The results indicated a uniform wall thickness distribution, with the maximum variation in thickness being 0.002 mm. Preform 1 had the largest wall thickness, and preform 3 had the smallest wall thickness. The difference between the thicknesses of preforms 1 and 3 was large but was still within the allowable range. The average thickness of the remaining preforms (i.e., preforms 2, 4, 5, and 6) was 0.948–0.963 mm, with the corresponding standard deviation being only 0.0014–0.0030 mm. The geometry of preform

1 barely differed from that of the corresponding bi-segment pressure hull (designated as hull 1). Therefore, only the thickness of this bi-segment pressure hull was measured and shown in Figure 5. The thicknesses of the remaining bi-segment pressure hulls (designated as hulls 2–6) decreased along the axis of rotation from the ends of the top and bottom shells toward the midpoint owing to the large amount of free bulging. Obviously, the midpoint of these hulls exhibited the smallest thickness.

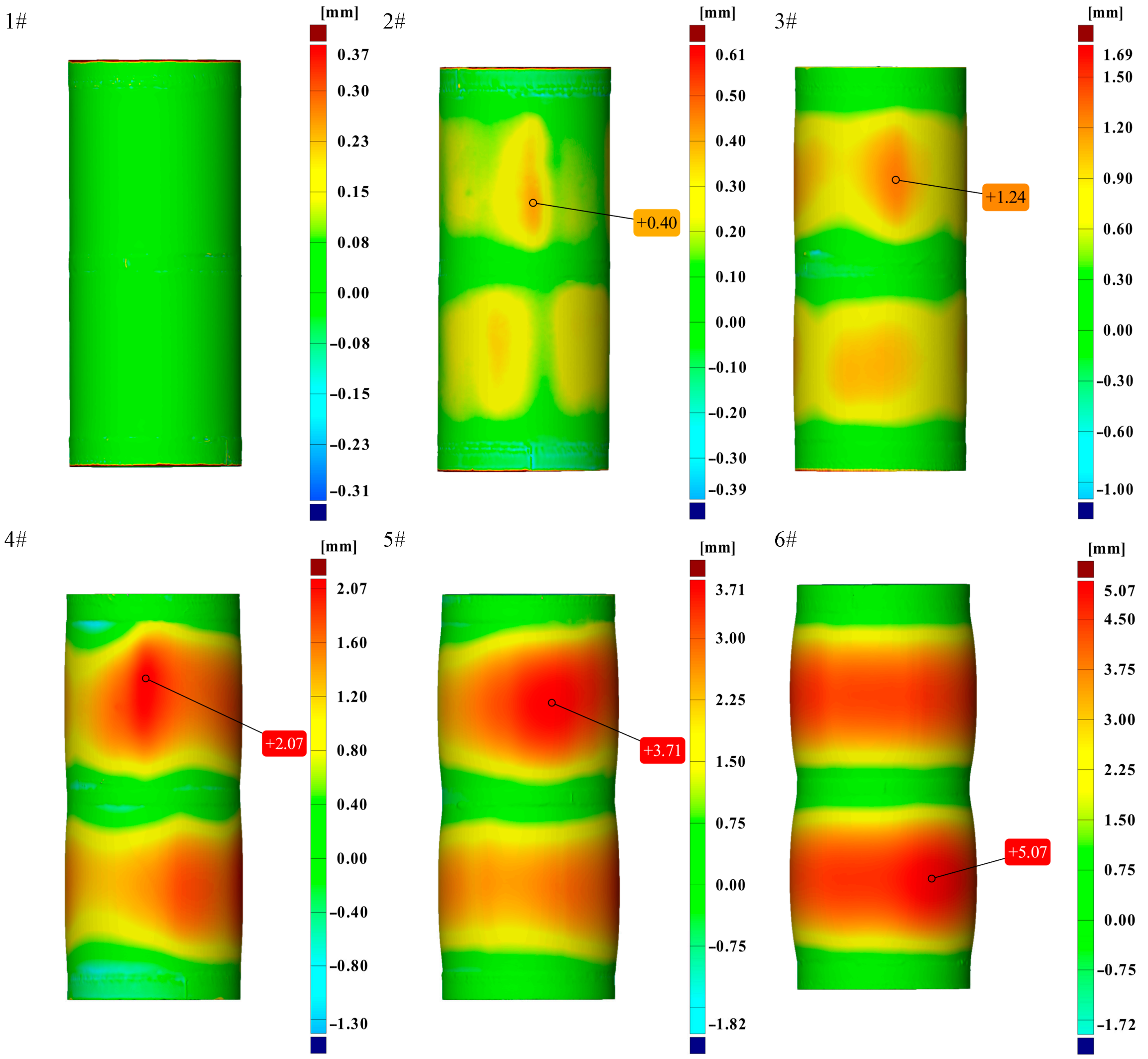

Figure 6. Shape deviations between bi-segment cylindrical preforms and the corresponding bulged hulls.

Table 4. Bulging magnitudes and growth rate of height of six test bi-segment cylindrical preforms.

Sample	ΔB_{ave} [mm]	ΔB_{max} [mm]	ΔH [%]
1#	0.000	0.00	0.01
2#	0.006	0.40	−0.01
3#	0.747	1.24	−0.06
4#	1.604	2.07	−0.25
5#	2.462	3.71	−0.34
6#	4.218	5.07	−0.47

Table 5. Maximum, minimum, and average thicknesses of bi-segment cylindrical performs and their corresponding standard deviations.

Sample		1#	2#	3#	4#	5#	6#
T_{max}[mm]	Top	0.972	0.958	0.938	0.968	0.952	0.956
	Bottom	0.970	0.958	0.936	0.966	0.954	0.958
T_{min} [mm]	Top	0.962	0.952	0.928	0.956	0.942	0.948
	Bottom	0.960	0.952	0.930	0.958	0.944	0.950
T_{ave} [mm]	Top	0.968	0.955	0.933	0.962	0.948	0.954
	Bottom	0.966	0.956	0.933	0.963	0.948	0.954
St.dev. [mm]	Top	0.0024	0.0014	0.0021	0.0021	0.0030	0.0015
	Bottom	0.0028	0.0015	0.0021	0.0020	0.0029	0.0020

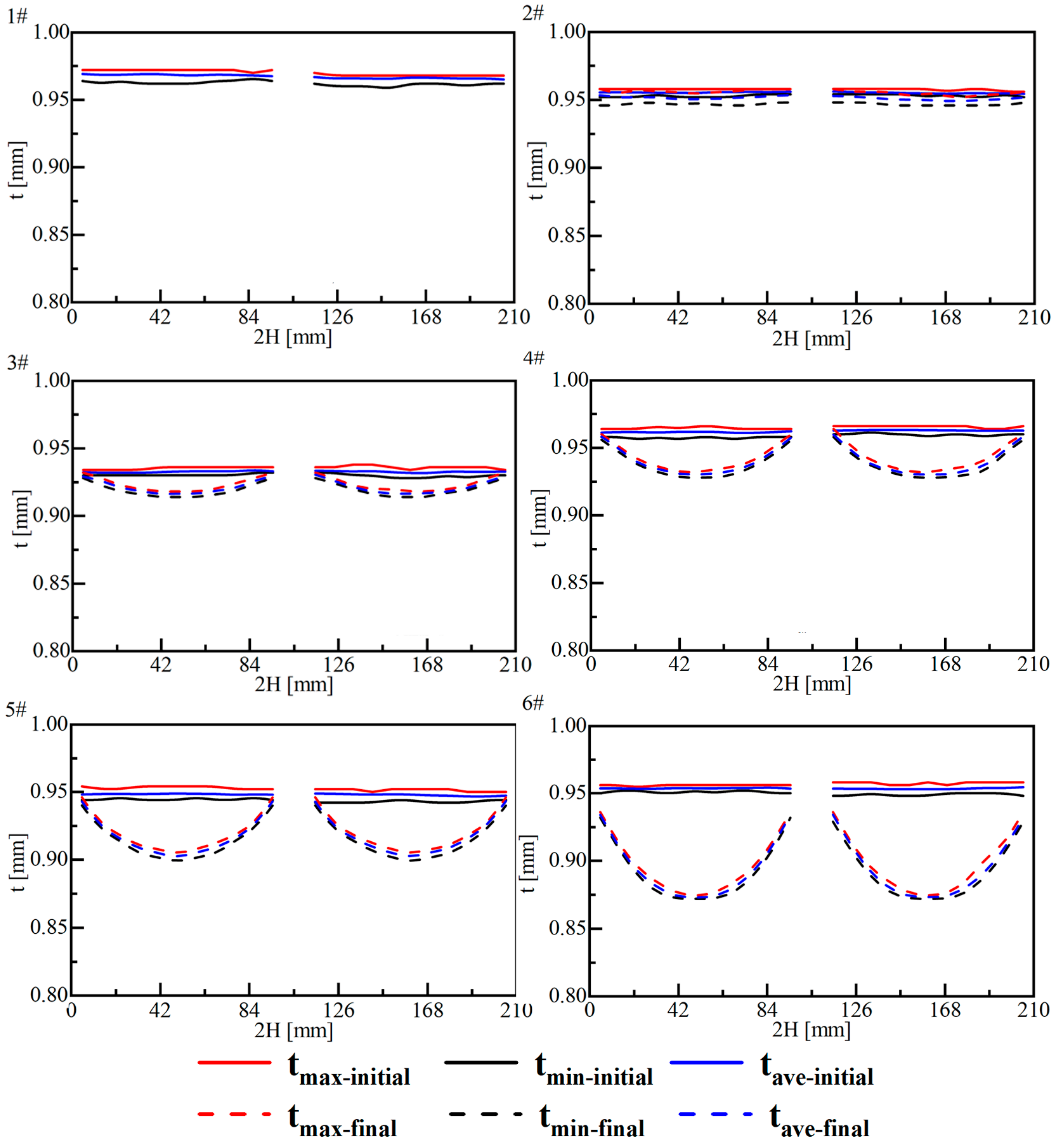

Figure 7. Thickness distributions of bi-segment cylindrical preforms (solid lines) and the corresponding bulged hulls (dotted lines).

2.2.2. Test Results

In the bulging test, we slowly injected tap water (used as the hydraulic medium) into each preform by using a manual water pump. We ensured that the entire bulging process was quasi static. It indicated that the bulging pressure increased with the bulging magnitude. Figure 8 illustrates the pressure histories, obtained from the internal free bulging tests, of preforms 2–6. As mentioned above, hull 1 was not subjected to free bulging and thus served as the reference (control). Because the pump was manually operated, the loading times varied considerably between hulls 2–6, as indicated by the pressure profiles. The maximum loading time was 180 s, and the minimum loading time was more than 24 s. This indicated that the loading process in the internal free bulging test was quasi static. The bulging loads for each hull are listed in Tables 5 and 6.

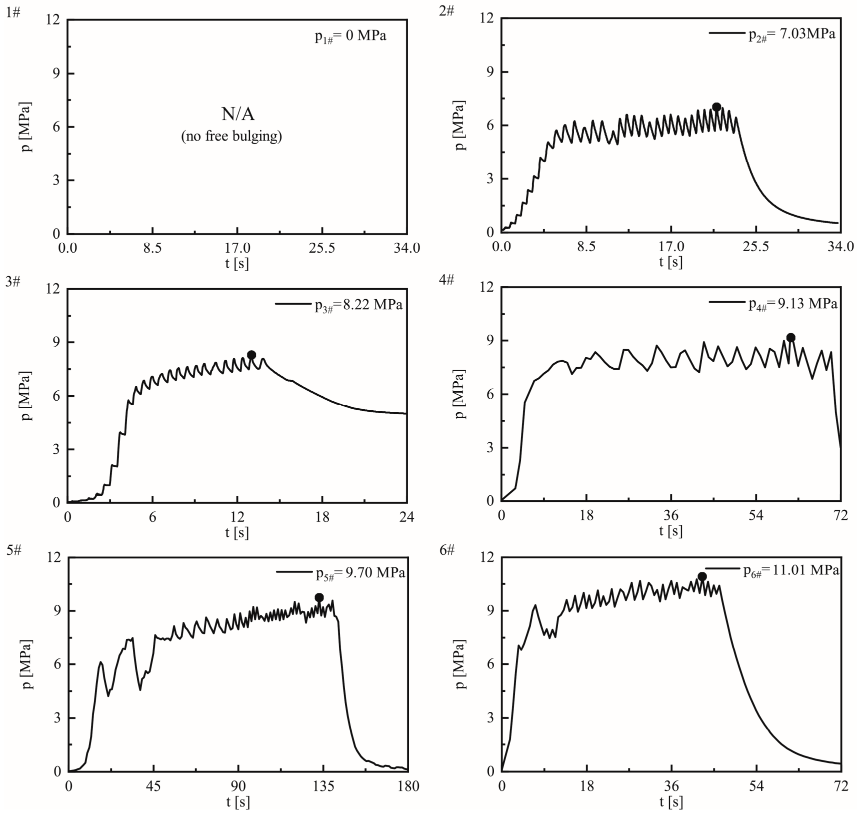

Figure 8. Pressure histories of five bi-segment cylindrical preforms during the free bulging process.

Table 6. Test time and loading rate of experiment.

Sample	*p* [MPa]	t_p [s]	p/t_p [MPa/s]	*P* [MPa]	t_P [s]	P/t_P [MPa/s]	*p*/*P*
1#	0.00	0	-	3.32	12	0.28	0.00
2#	7.03	22	0.32	3.55	6	0.59	1.98
3#	8.22	13	0.63	3.33	12	0.28	2.47
4#	9.13	61	0.15	3.68	51	0.07	2.48
5#	9.70	133	0.07	3.90	27	0.14	2.49
6#	11.01	42	0.26	4.54	24	0.19	2.43

Notably, preform 1 was considered a special case with an infinite radius in the meridional direction. It was not subjected to bulging (i.e., 0 MPa was applied to it), and the remaining preforms were subjected to bulging under loads of 7.03, 8.22, 9.13, 9.70, and 11.01 MPa, separately. The loading process was divided into three stages. During the initial stage, the entire preform was completely filled with running water (the pressure medium) by using the manual water pump. When the curve was in the middle stage, internal pressure was uniformly applied to induce the initial bulging of the hull. Until the final stage, an internal pressure was slowly applied to induce complete free bulging. The bulging times of hulls 2–6 ranged from 13 to 133 s, and the bulging rates ranged from 0.07

to 0.63 MPa/s. Thus, the entire free bulging process was quasi–static. The bulging loads, times, and rates are listed in Table 6.

After the free bulging test, six bi-segment pressure hulls were obtained. These bi-segment pressure hulls were also subjected to an external hydrostatic pressure test, which was divided into three stages (Figure 9). The hydrostatic test entailed pressurising the hulls under external hydrostatic pressure. The results revealed that the hulls collapsed due to the applied pressure. Similar to the bulging pressure, the buckling pressure increased with the bulging load. Specifically, the buckling pressure of the bi-segment cylindrical hulls increased with the bulging load (Table 6). The buckling pressure of bi-segment pressure hull 1 was 3.32 MPa, and those of bi-segment pressure hulls 2, 3, 4, 5, and 6 were 3.55, 3.33, 3.68, 3.90, and 4.54 MPa, respectively. The pressurisation times ranged from 6 to 51 s, and the pressurisation rates ranged from 0.07 to 0.59 MPa/s. Compared with that of hull 1, the buckling pressure of hull 6 was improved by 36.75%.

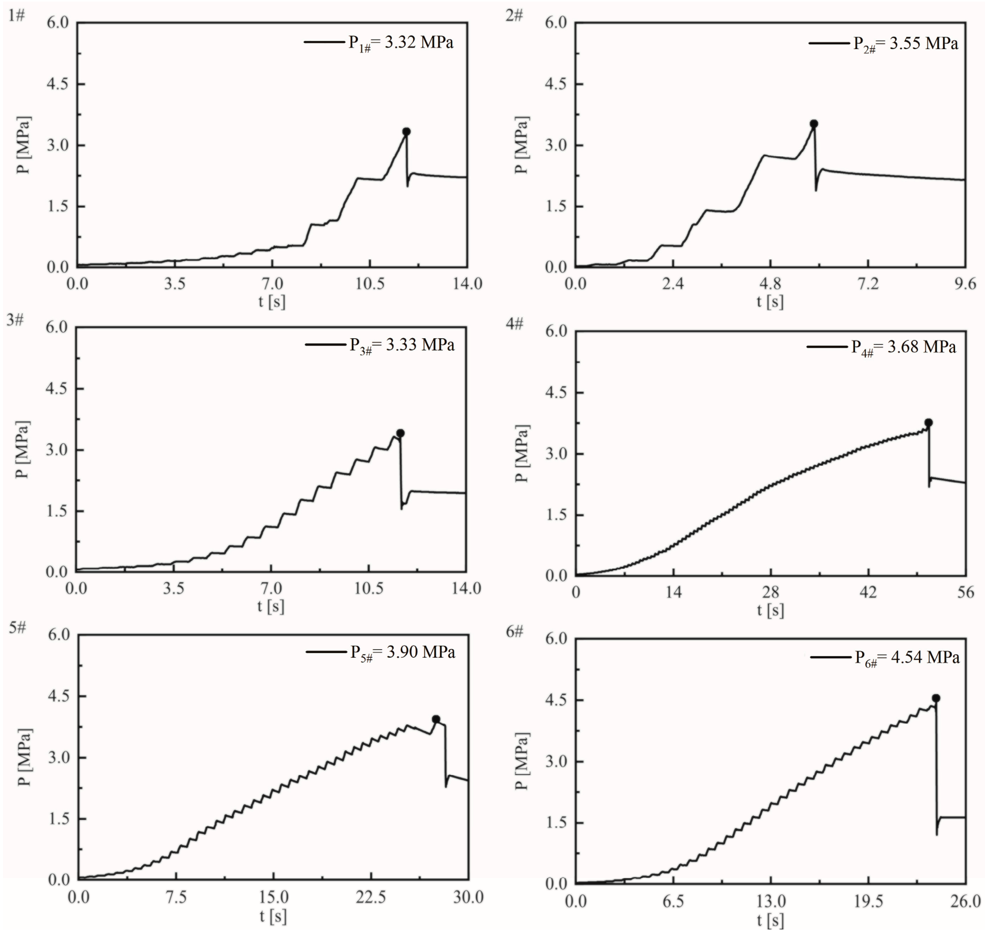

Figure 9. Pressure histories of one bi-segment cylindrical preform (preform 1) and five bi-segment bulged hulls (hulls 2–6) during hydrostatic tests.

The typical failure mode of bisegment pressure hulls is characterised by a local collapse [17–21]. In this study, the failure modes of the six hulls were characterised by local pits, as displayed in Figure 10. In this figure, the failure areas were indicated by the red circles. Hulls 1–3 subjected to low bulging loads exhibited pits at their bottom sections. This phenomenon was mainly because the relatively low bulging loads failed to remedy the preform shape deviations of these samples. Hulls 4–6 exhibited depressions at their top sections. The reason for these depressions is provided as follows: the shape of the shells changed from cylindrical to bi-segment pressure hulls as the bulging load increased. When the bulging pressure was large, the thicknesses of the shells decreased and the material hardened. Consequently, the uneven thickness distribution and material hardening resulted in the one-sided destabilisation.

Figure 10. Bi-segment collapsed cylindrical preform (preform 1) and bulged hulls (hulls 2–6) after the hydrostatic tests.

3. Numerical Analysis

This section presents a numerical analysis of the free bulging performance of a bi-segment cylindrical preform under internal pressure and the buckling properties of the resulting hulls under external pressure. The section first presents the numerical modelling process and then the numerical results, including bulging and buckling analysis results, which were compared with the experimental results.

3.1. Numerical Modelling

Nonlinear FEM was applied using ABAQUS to further explore the bulging and buckling capacities of the preform and the resulting hulls, respectively. The nominal dimensions of the samples were used as the parameters of the established numerical model, and the bisegment cylindrical preform was modelled as an axisymmetric shell. Specifically, in the modelling process, this shell was considered to be axisymmetric along its meridian for computational convenience. The numerical simulation was involved three steps (Figure 11): (1) free bulging, (2) springback, and (3) external pressurisation. The thickness-to-diameter ratio of the bi-segment cylindrical preform was only 0.0093, as evaluated by the ABAQUS/Standard nonlinear static solver that was executed in the first and second steps of the simulation.

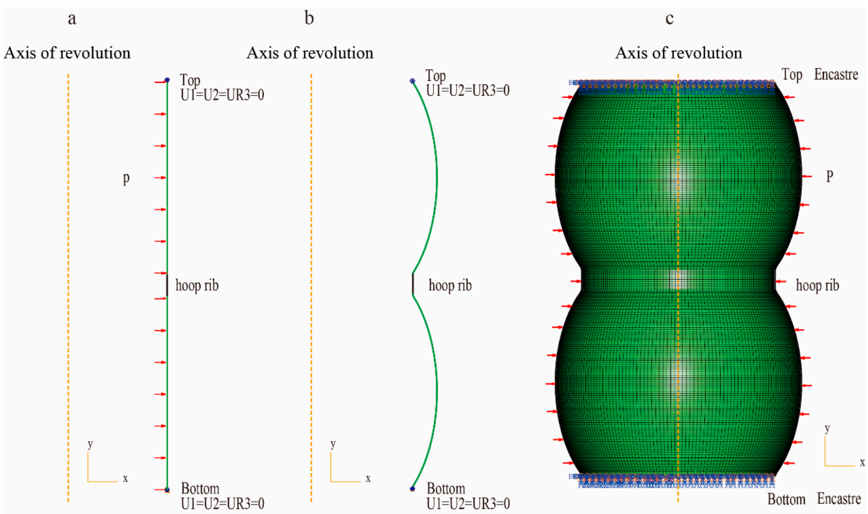

Figure 11. Finite-element models of free bulging (**a**), springback (**b**), and external pressurisation (**c**).

From the axisymmetric shell element library of ABAQUS/Standard, two-node shell (SAX1) elements were used to establish the numerical model of the bi-segment cylindrical preform. A one-dimensional linear numerical model was divided into 213 axisymmetric nodes (Figure 11). To simulate the closed constraints of the two thick plates and the hoop rib on the numerical model, the top and bottom points of the model were completely fixed, and the hoop rib nodes were given full degrees of freedom, which was the same as a previous study [31]. The maximum values for bulging magnitude ΔB for the numerical model were set to 0, 1, 2, 3, 4, 5, and 6 mm. Figures 12–15 show the geometrical and mechanical properties observed for the bulged and springback models.

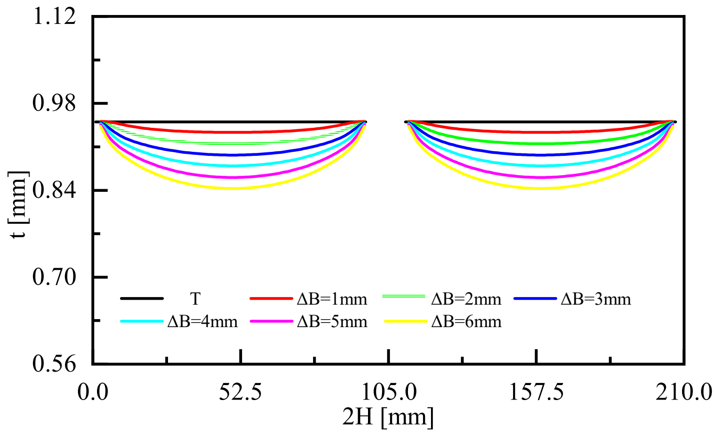

Figure 12. Thickness distributions of the bi-segment bulged hulls obtained from numerical analysis.

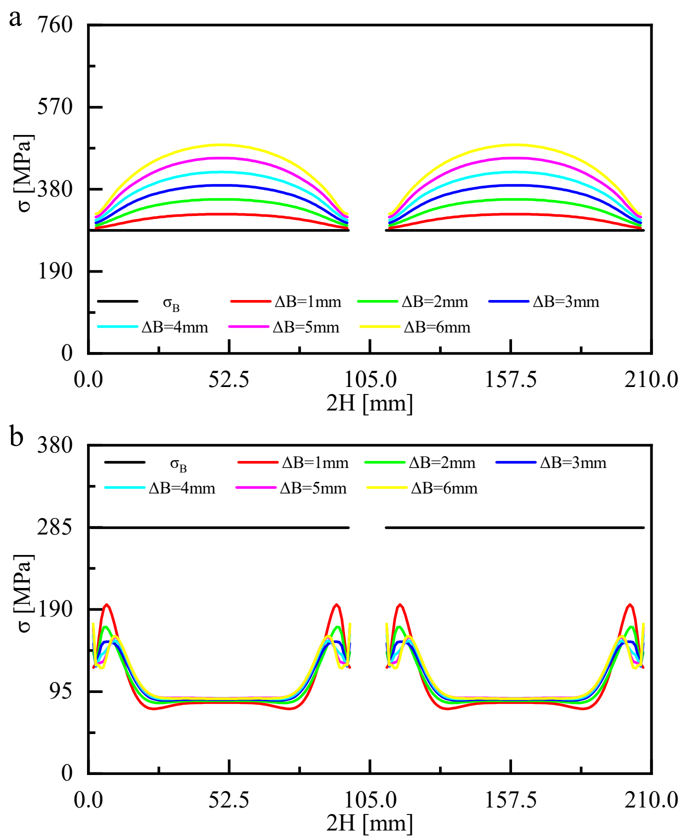

Figure 13. Von Mises stress (**a**) and residual stress (**b**) of bi-segment bulged hulls with various bulging magnitudes as obtained from numerical analysis.

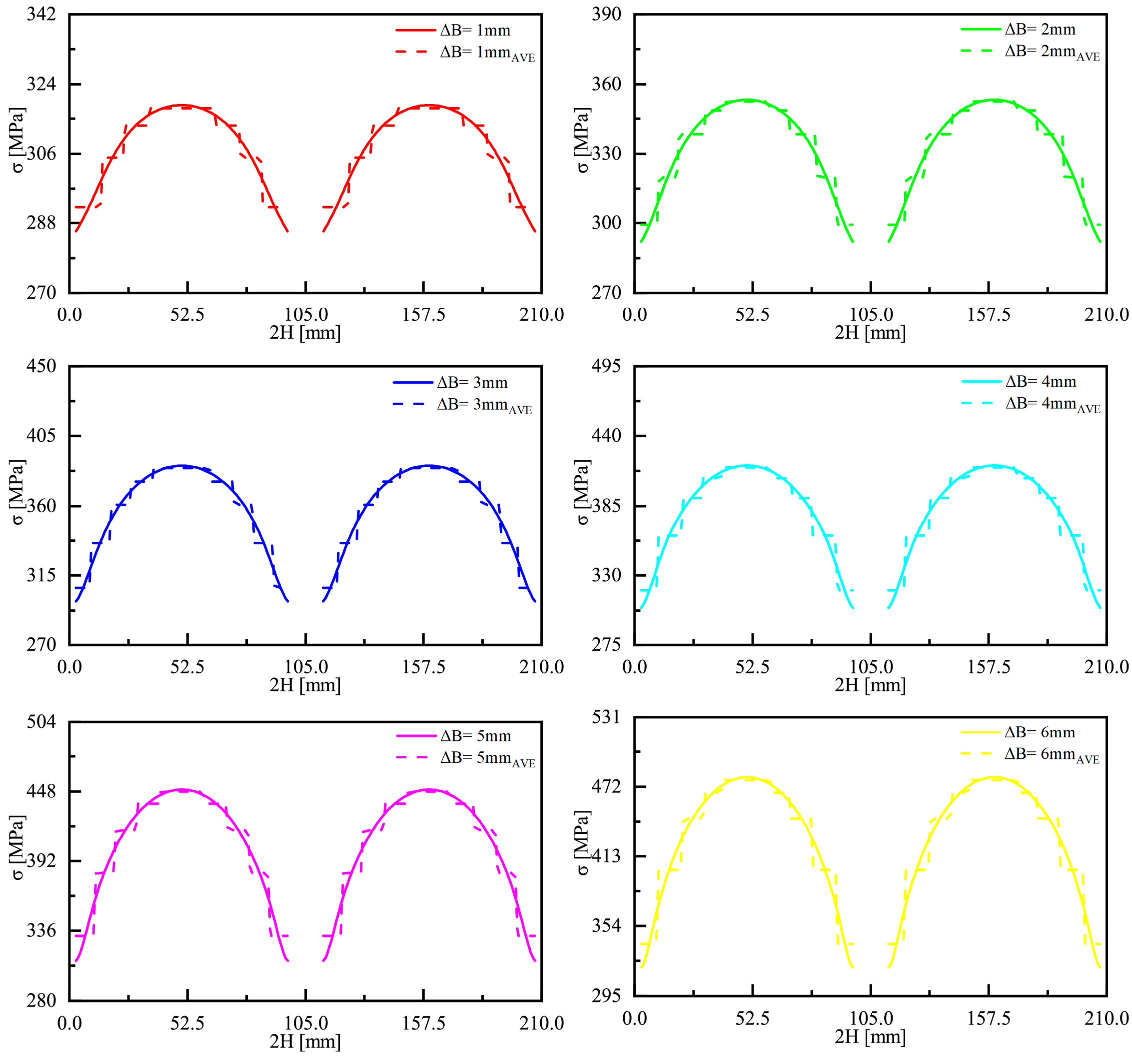

Figure 14. Average yield points (dotted lines) defined according to the bulging calculations (Figure 13a) indicated by the solid lines.

The springback model (Figure 11b) was rotated to derive a 3D model (Figure 11c), and the geometrical and material properties of the derived model were assessed through nonlinear FEM. The finite element meshes in the 3D model were obtained by rotating 213 isometric deformed finite element meshes. Thus, the mesh and node numbers for the seven bi-segment pressure hulls were 42,600 and 42,400, respectively. The converted meshes were determined to be linear quadrilateral elements (S4R), and the number of meshes was verified by convergence, as shown in Figure 16. The thickness of each bi-segment pressure hull was defined as a function of the bulging magnitude obtained after the springback step (Figure 13). Because of plastic deformation induced by the free bulging process, the material of the bi-segment cylindrical hull was hardened.

For each hull, the yield stress was uniformly distributed in the circumferential direction and nonuniformly distributed in the meridional direction (Figure 13). The Von Mises stress and residual stress of the bi-segment pressure hulls under various bulging magnitudes are shown in Figure 13. Similar to the observed thickness distribution, the maximum stress was observed at the midpoints of the top and bottom hulls and then decreased symmetrically along the axial direction toward the ends of the hulls (Figure 13a). We also observed that during the free bulging process, the hardening of the bi-segment cylindrical hull material increased with the bulging magnitude. Moreover, the equivalent stress on the hulls decreased as the bulging pressure decreased gradually (Figure 13b), indicating that the free bulging process was quasi static. Nevertheless, some residual stress was still observed. Regarding the residual stress distribution, we observed the minimum stress values at the midpoint of the top and bottom shells of the bi-segment pressure hulls, and the stress subsequently increased axially toward the ends of the hulls. This phenomenon could be attributed to the complete constraints imposed on the hull ends (Figure 11) and to the thickness reduction (Figure 12). A previous study reported that shell material hardening and an increase in curvature could increase the buckling capacity of a shell [30].

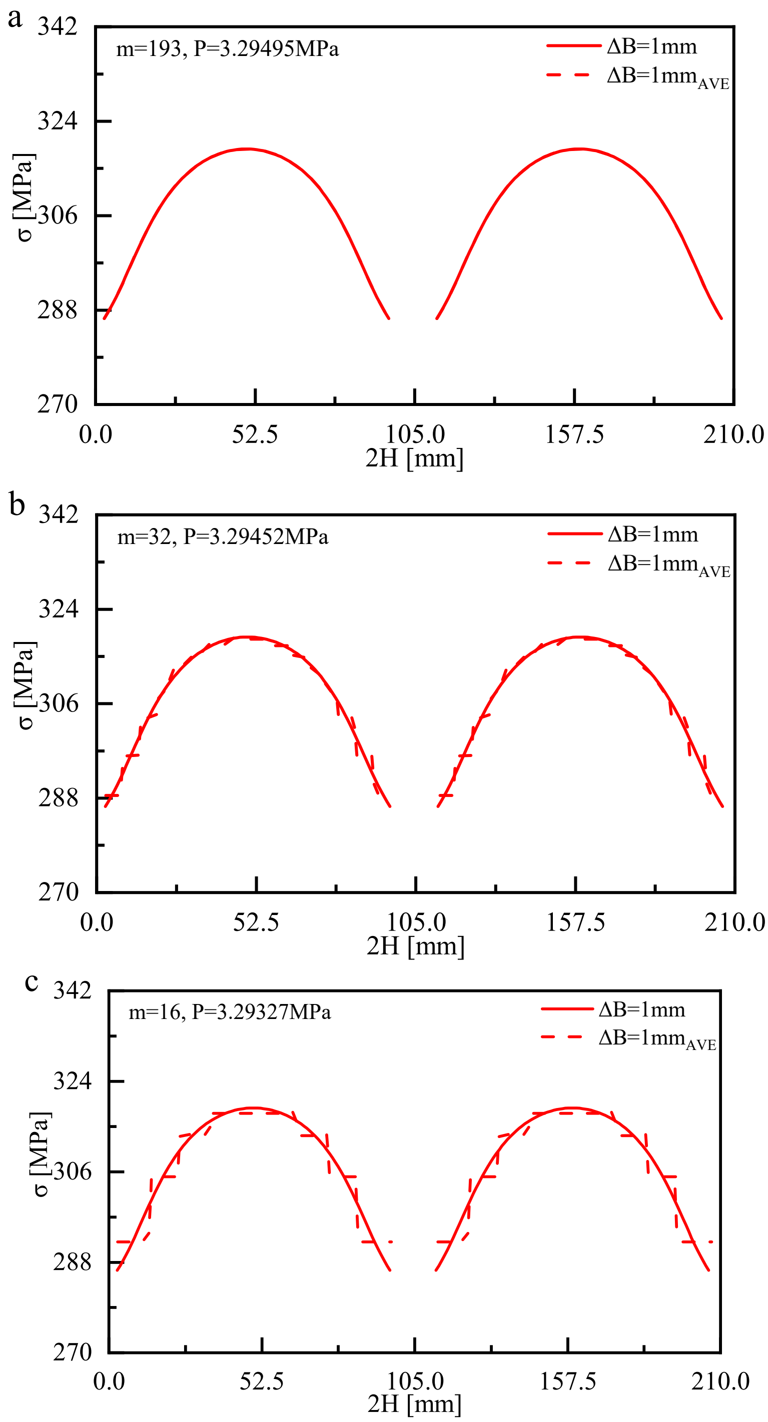

Figure 15. Typical example of division segments (m) used for the convergence analysis. (**a**) m = 193; (**b**) m = 32; (**c**) m = 16.

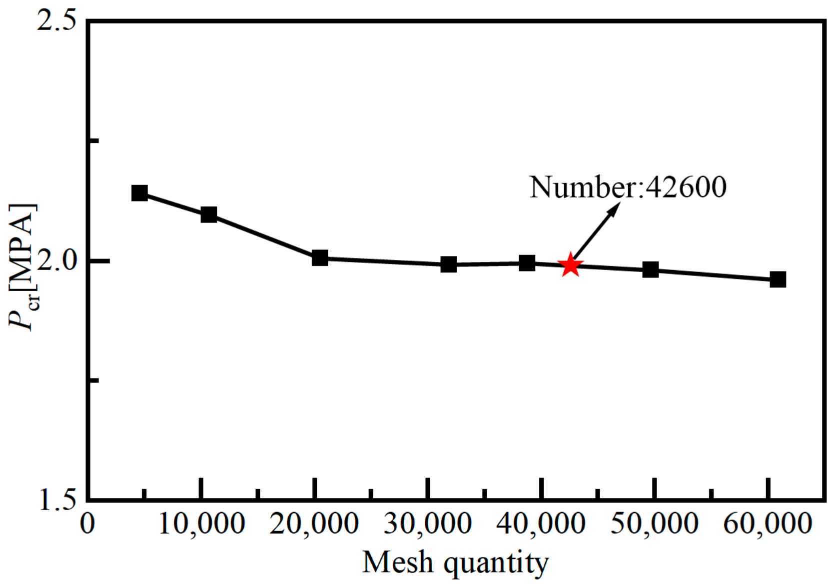

Figure 16. Convergence study of the bi-segment bugled hulls.

Accordingly, the average yield point was redefined in each circular region (Figure 14). For example, for $\Delta B = 1$ mm, three-line segments were used for nonlinear buckling analysis (Figure 15), and the predicted buckling loads for these segments were 3.29495, 3.29452, and 3.29327 MPa, demonstrating convergence. This result is consistent with that of a previous study on the buckling properties of bulged hulls under external pressure [30]. To simulate the external pressure exerted on bi-segment pressure hulls in practical scenarios, the ends of the hulls were constrained as a boundary condition, which was similar to a previous study [35]. In addition, a unit pressure of 1 MPa was uniformly applied to the outer surfaces of the hulls. This pressure served as the reference load for the numerical analysis of nonlinear buckling and did not influence the results. The first-order eigenmode of the bi-segment pressure hulls was introduced as initial geometric imperfections, with the selected imperfection sizes being $0.1T$, $0.2T$, and $0.3T$. Furthermore, linear elastic eigenvalues were evaluated through a structural analysis to determine the eigenmode and linear buckling loads for each hull.

3.2. Numerical Results and Discussion

3.2.1. Bulging Analysis

The deformed geometries of the bi-segment pressure hulls for different bulging magnitudes (ΔB) are illustrated in Figure 17. For the preform without carrying out free bulging, a relatively straight profile was observed. In contrast, curved profiles of the bi-segment pressure hulls under uniform internal pressure were observed. The hoop rib was not displaced, and the hull profiles appeared as bicircular arcs whose curvature increased with the bulging magnitude. The correlation coefficient for the fitted radius of curvature (r)—derived using Origin software—was between 99.50% and 99.79%, demonstrating the validity of the fit and the practicality of the model design.

The radius of curvature r decreased with the bulging magnitude (Figures 17 and 18d). Previous studies on the free bulging of thin-walled cylinders [29,30] have presented an analytical equation for the meridional radius of curvature of such cylinders. We adapted this equation to the present study, as presented in Equation (10).

$$R = \frac{\Delta B^2 + \left(\frac{H}{2}\right)^2}{2\Delta B} \tag{10}$$

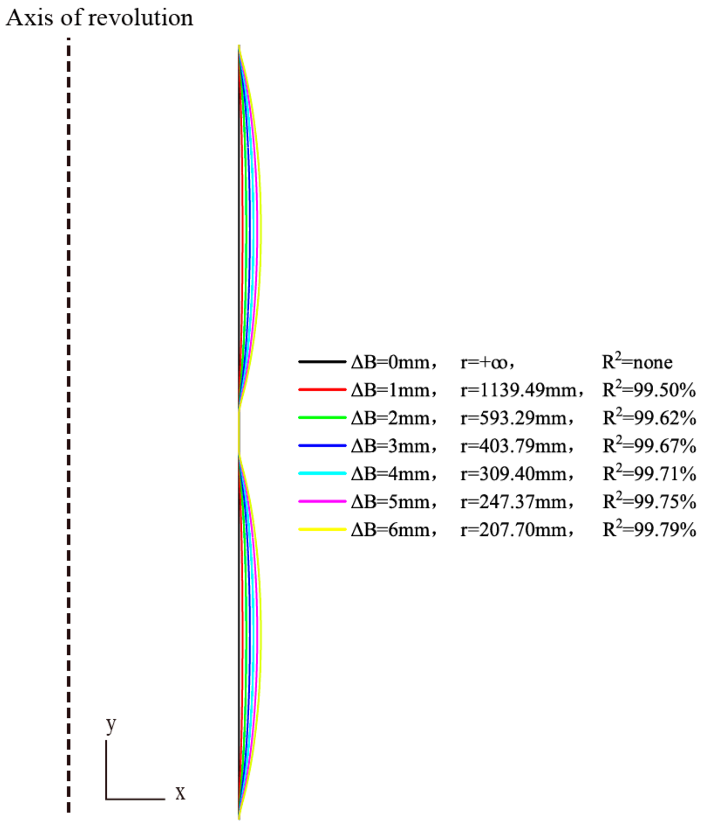

Figure 17. Deformed meridians of bi-segment pressure hulls with various bulging magnitudes obtained from numerical analysis, where r is the fitted radius of each curve and R^2 is the coefficient of determination.

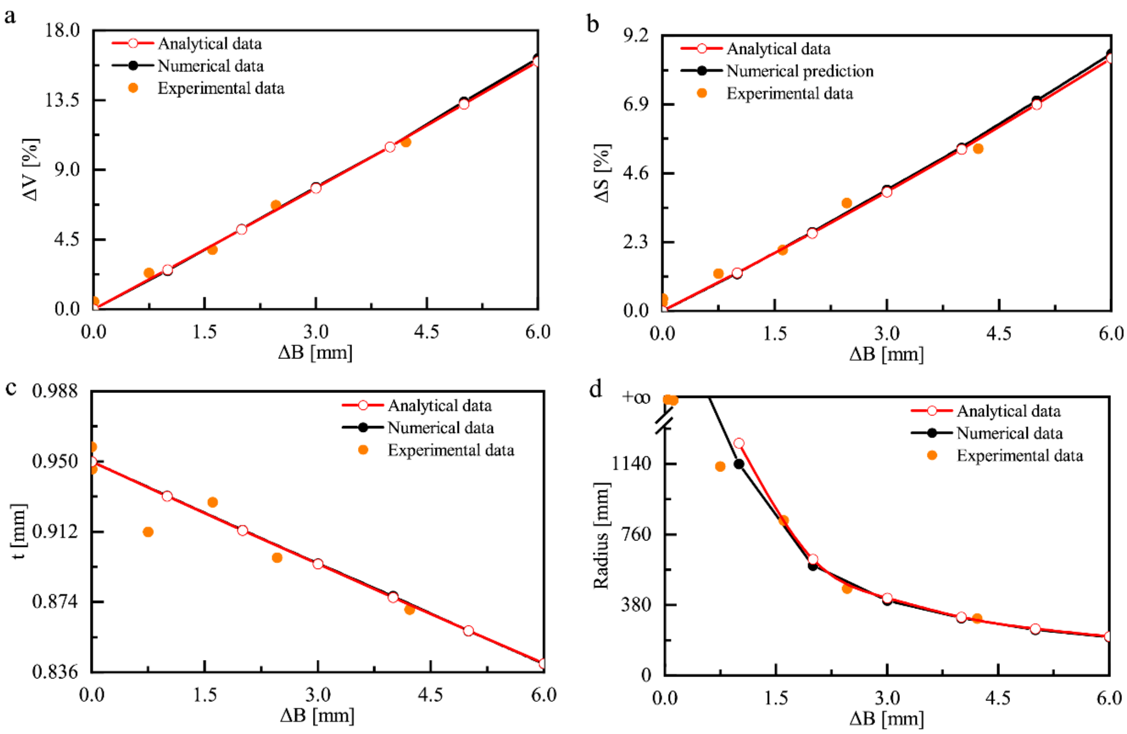

Figure 18. Plots of volume increment (**a**), area increment (**b**), minimum thickness (**c**), and meridian radius (**d**) versus the bulging magnitude of the bi-segment bulged hulls.

We observed that the analytical results were in good agreement with the numerical and experimental results. We also used Equations (11) and (12) to calculate the growth rate of the volume and external area of the bi-segment pressure hulls. We determined that the growth rate of the volume and external surface area of the bi-segment pressure hulls increased monotonically with the bulging magnitude (Figure 18a,b). It can be seen that the maximum growth rate of the volume and surface area of the hulls were 16.21% and 8.60%, respectively. Accordingly, the obtained analytical, numerical, and experimental results were in good agreement [29].

$$V = \int_{-\frac{H}{2}}^{\frac{H}{2}} \pi \left[\sqrt{R^2 - x^2} - \left(R - \Delta B - \frac{D}{2} \right) \right]^2 dx \tag{11}$$

$$S = \int_{-\frac{H}{2}}^{\frac{H}{2}} 2\pi \left| \sqrt{R^2 - x^2} - \left(R - \Delta B - \frac{D}{2} \right) \right| \sqrt{1 + \left[\sqrt{R^2 - x^2} - \left(R - \Delta B - \frac{D}{2} \right)' \right]^2} dx \tag{12}$$

When the hull mass was kept constant, the minimum hull thickness decreased linearly as the bulging magnitude increased (Figure 18c). The plots of thickness versus height are display in Figures 13 and 18c. The simulated thicknesses of the top and bottom shells of the bi-segment pressure hulls exhibited consistent trends, decreasing from the ends of the shells toward the middle of the shells. The minimum thickness was observed at the midpoint of each hull, and the maximum reduction rate was 11.53%. Accordingly, the analytical results regarding minimum thickness were in agreement with the numerical and experimental results, as indicated in Equation (13) [29].

$$t = \left(2.79154E - 06\Delta B^3 - 2.92802E - 04\Delta B^2 - 1.39745E - 04\Delta B + 1 \right) \frac{(D/2)T}{R} \tag{13}$$

3.2.2. Buckling Analysis

The buckling loads of the bi-segment pressure hulls exhibited a bilinear increase as the bulging magnitude increased. Specifically, the linear buckling loads increased with the bulging magnitude, as illustrated in Figure 19a. The buckling variation in the bi-segment pressure hulls can be attributed to their increased bulging curvature, reduced thickness, and elastic properties. Figure 19b presents the normalised buckling loads of the preform and the six bi-segment pressure hulls, as derived from numerical and experimental analyses. The normalised buckling loads increased linearly with the bulging magnitude. Notably, the buckling loads predicted for the three aforementioned imperfections ($0.1T$, $0.2T$, and $0.3T$) by using nonlinear FEM were in good agreement with the linear predictions. Accordingly, the experimental data were in good agreement with the linear predictions.

The numerically simulated linear buckling modes of the bi-segment pressure hulls are shown in Figure 20. These modes were obtained using multiple latitudinal waves and half of a meridional wave. We observed that the value of the latitudinal wave (n) increased with the bulging magnitude for each bisegment cylindrical hull and was located at the middle of the thinnest sections of the top and bottom shells of the hull; this can be attributed to the increase in the radius-to-thickness ratio along the latitudinal direction of the bi-segment cylindrical hulls. Specifically, the value of the latitudinal wave (n) increased from 24 for the preform to 32 for the bisegment cylindrical hull ($\Delta B = 6$ mm).

In our nonlinear numerical analysis, we used the first-order linear buckling mode obtained from the evaluation of the linear elastic eigenvalues as the initial geometric imperfection, in accordance with the EN 1993-1-6 (2007) [36] and CCS 2018 [37] guidelines. Moreover, in the nonlinear numerical analysis, we considered the hulls to exhibit increased bulging curvature, reduced thickness, and elastic material properties, similarly to the linear numerical analysis. The equilibrium paths derived for the bi-segment pressure hulls from our numerical analysis at an imperfection size of $0.2T$ are presented in Figure 21. These paths revealed an unstable post-buckling regime. For the bi-segment pressure hulls with bulging magnitudes of 0–6 mm, the equivalent stress observed in the buckling region (i.e., pit generation region) was greater than the material yield stress, indicating a nonlinear elastic–plastic buckling regime. This finding is consistent with the findings of previous studies on the buckling properties of bulged barrels under external pressure [29,30]. The displacement in Figure 21 represents the maximum displacement in the buckling (pit) region. Before the critical buckling point, the pressurisation rates applied to the hulls increased nonlinearly. After the critical buckling point, the applied rates decreased suddenly owing to the instability of the hulls.

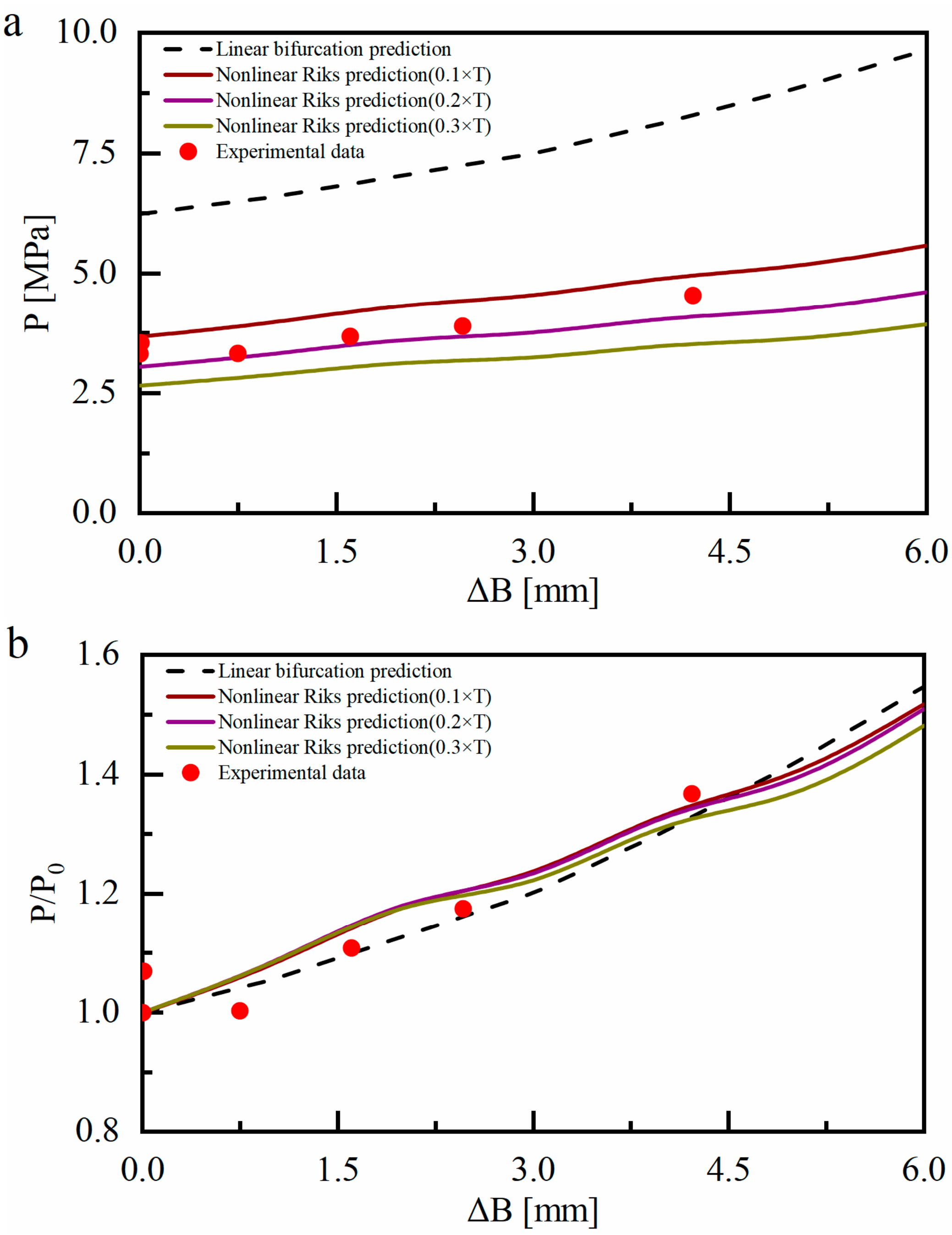

Figure 19. Buckling loads (**a**) and their normalised values (**b**) for one preform and five bi-segment bulged hulls obtained from numerical and experimental analyses.

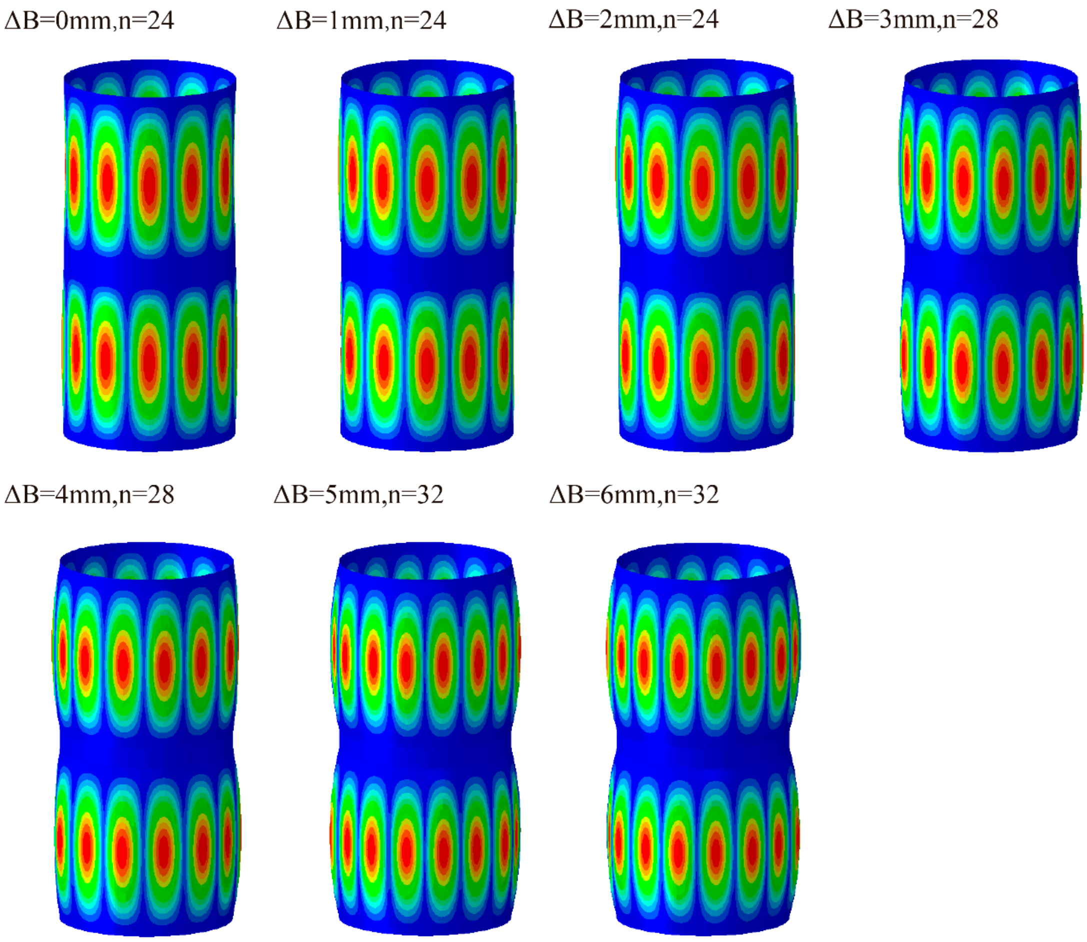

Figure 20. Linear buckling modes of bi-segment bulged hulls as obtained from numerical analysis.

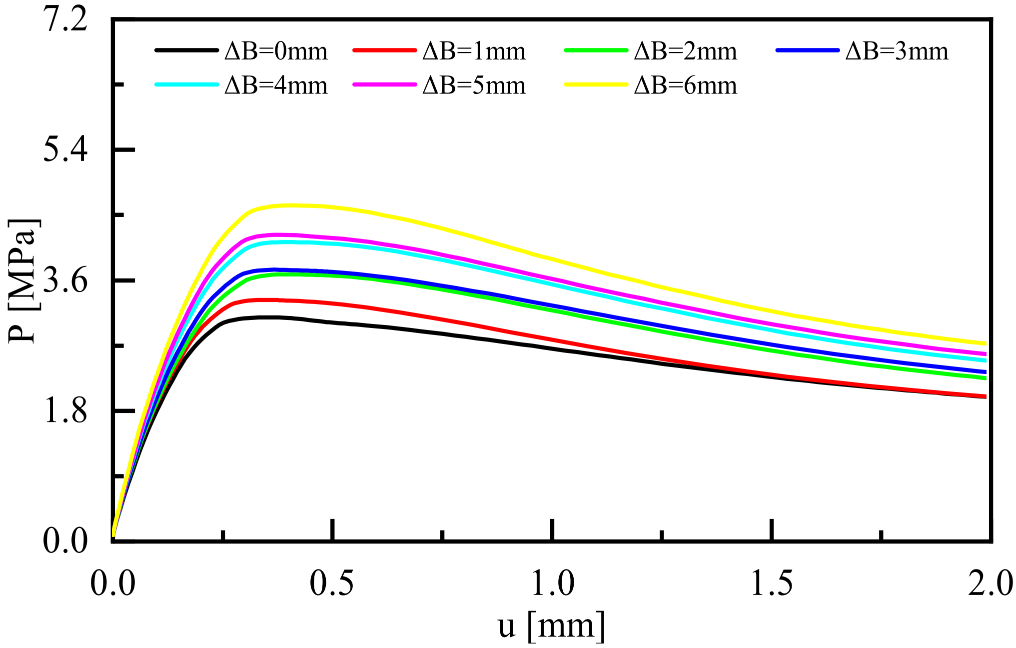

Figure 21. Equilibrium paths of bi-segment bulged hulls as obtained from numerical analysis at an imperfection size of 0.2T.

In summary, the nonlinear post-buckling modes observed for the bi-segment pressure hulls at an imperfection size of 0.2T were characterised by one or two local pits. These unstable postbuckling properties and local postbuckling modes are typical of rotating steel shells under uniform external pressure [17–21]. In this study, when $\Delta B = 1$ and 3 mm, local pits were distributed in the top and bottom shells of the bi-segment pressure hulls, respectively. This indicates that initial geometrical imperfections were the main factors influencing the buckling modes of the hulls. For the remaining bi-segment pressure hulls, the buckling modes were characterised by a pit on one side of each hull, which can be attributed to the uneven thickness distribution for these hulls. When $\Delta B > 3$ mm, local pits occurred at the bottom end of each bi-segment pressure hull. Preform material hardening occurred during the bulging process. Hence, we included this hardening effect along with thickness reduction and curvature enhancement in our nonlinear numerical analysis. As shown in Figure 19, the trend of the nonlinear buckling loads corresponding to the critical buckling point was similar to that observed in the linear numerical analysis; the loads increased linearly with the bulging magnitude. In addition, the numerical findings displayed in Figure 22 are consistent with the experimental results displayed in Figure 10, indicating that material hardening played a major role in enhancing the buckling capacity of the bi-segment pressure hulls.

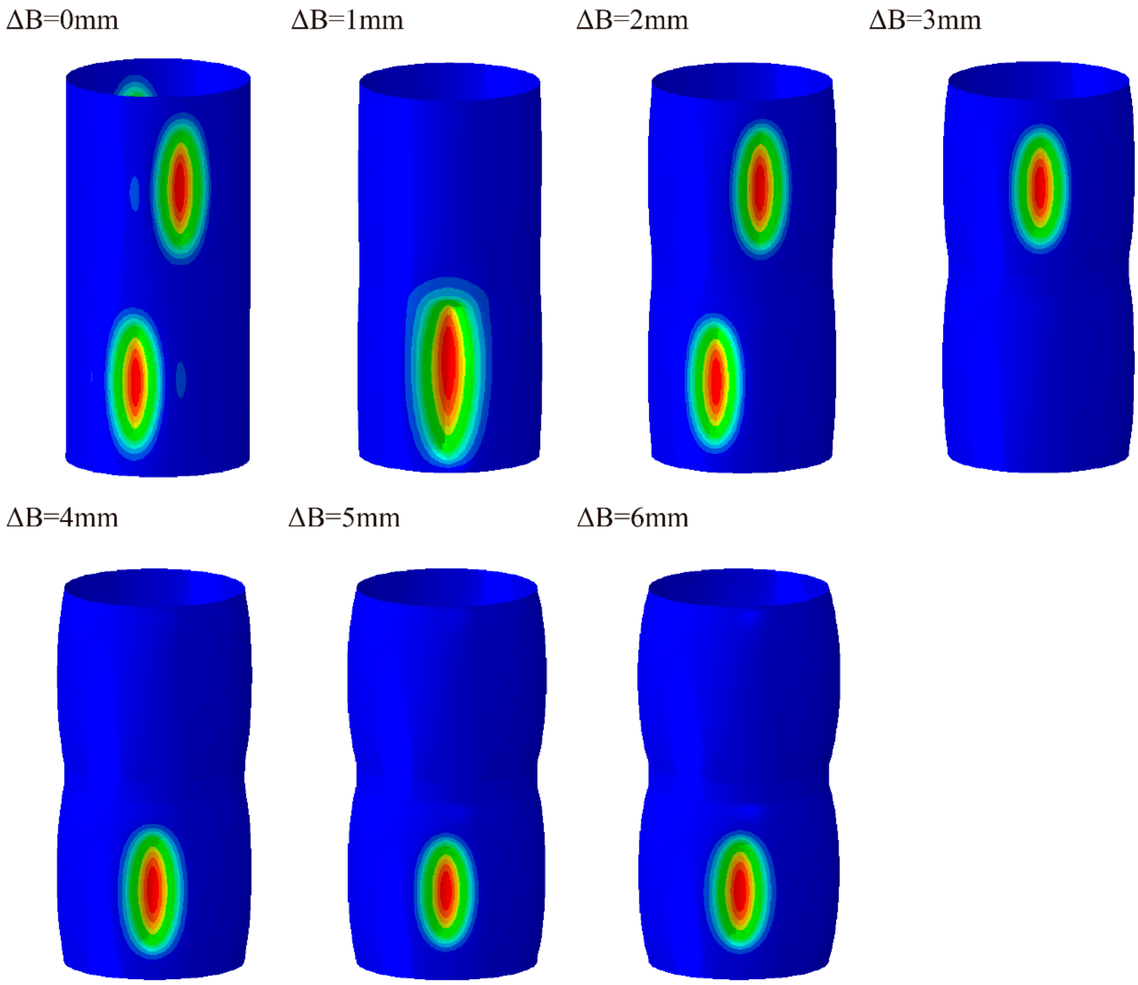

Figure 22. Nonlinear post-buckling modes of bi-segment bulged hulls obtained from numerical analysis at an imperfection size of 0.2T.

4. Conclusions

This study experimentally and numerically investigated the buckling properties of bi-segment pressure hulls under hydrostatic pressure. The main conclusions are outlined as follows:

(1) Six bi-segment cylindrical preforms were fabricated through the TIG technique and exhibited favourable symmetry and machinability. Owing to the thick steel plates at the ends of the preforms, six bi-segment cylindrical hulls were produced through a quasi–static free bulging process; the hulls exhibited favourable geometric symmetry and a favourable thickness distribution around the axis of rotation. The hoop rib was not displaced during the free bulging process, and this can be attributed to the deformation consistency of the hulls. This thus verifies the reliability of the design parameters.

(2) Free bulging increased the volume and surface area and decreased the thickness of a bi-segment pressure hull. This study revealed that the maximum bulging magnitude for the bi-segment pressure hulls was 4.218 mm. The hulls had a volume growth rate of 10.81%, surface area growth rate of 5.43%, and maximum thickness reduction of 11.58%.

(3) The buckling loads of the six bi-segment pressure hulls produced in this study increased with the bulging magnitude under uniform hydrostatic pressure. Compared with buckling load of the control preform (preform 1) that was not subjected to a bulging load, the buckling loads of the other bulged hulls were increased by 6.93%, 0.31%, 10.84%, 17.47%, and 36.75%. The buckling modes of the bi-segment pressure hulls were characterised by local pits, whose location was related to the initial geometrical imperfections of the preform and the thickness distribution after free bulging.

(4) Our numerical analysis of free bulging revealed that the growth rates of the volume and surface area of the bi-segment pressure hulls and the reduction rate of the thinnest points of the bi-segment pressure hulls increased linearly with the bulging magnitude. In contrast, the radius of the meridian decreased as the bulging magnitude increased. The numerical simulation results were in good agreement with the experimental and analytical results.

(5) Our numerical buckling analysis indicated that the external pressure buckling capacity of the bi-segment pressure hulls fabricated through free bulging was relatively high. Both the linear and nonlinear buckling loads of the bi-segment pressure hulls increased linearly with the bulging magnitude. The linear buckling modes were observed using 24–32 latitudinal waves and half of a meridional wave. The nonlinear buckling modes were characterised by two local pits under low bulging magnitudes and by a single local pit under large bulging magnitudes.

In this study, we considered only the buckling of bi-segment pressure hulls that were fabricated through free bulging and subjected to external hydrostatic pressure. To extend the application of our findings to other structures of deep-sea space stations, future studies should explore the buckling behaviour of multi-cone, multi-sphere, and other positive Gaussian curvature shells that are fabricated through free bulging and subjected to external pressure.

Author Contributions: Y.T. and J.Z. equally contributed to this work. Conceptualization, J.Z.; methodology, J.Z. and F.W.; software, Y.T.; validation, F.W.; formal analysis, J.Z.; investigation, Y.T. and J.Z.; data curation, Y.T.; writing—original draft preparation, Y.T.; writing—review and editing, J.Z.; All authors have read and agreed to the published version of the manuscript.

Funding: This study was supported by the National Natural Science Foundation of China [grant numbers: 52071160 and 52071203], Excellent Youth Foundation of Jiangsu Scientific Committee [grant number: BK20190103], Six Talent Climax Foundation of Jiangsu [grant number: KTHY-068].

Institutional Review Board Statement: Not applicable.

Informed Consent Statement: Not applicable.

Data Availability Statement: All data are included in the manuscript.

Conflicts of Interest: The authors declare no conflict of interest.

References

1. Craven, R.; Graham, D.; Dalzel-Job, J. Conceptual Design of a Composite Pressure Hull. *Ocean Eng.* **2016**, *128*, 153–162. [CrossRef]
2. Carlisle, T.F. *Ross Pressure Vessels External Pressure Technology*, 2nd ed.; Elsevier: Amsterdam, The Netherlands, 2011.
3. Błachut, J.; Smith, P. Buckling of Multi-Segment Underwater Pressure Hull. *Ocean Eng.* **2008**, *35*, 247–260. [CrossRef]
4. Błachut, J. Buckling of Externally Pressurised Barrelled Shells: A Comparison of Experiment and Theory. *Int. J. Press. Vessel. Pip.* **2002**, *79*, 507–517. [CrossRef]
5. Błachut, J. Experimental Perspective on the Buckling of Pressure Vessel Components. *Appl. Mech. Rev.* **2014**, *66*, 30–33. [CrossRef]
6. Bałchut, J.; Wang, P. Buckling of Barreled Shells Subjected to External Hydrostatic Pressure. *J. Press. Vessel Technol. Trans. ASME* **2001**, *123*, 232–239. [CrossRef]
7. Błachut, J. Combined axial and pressure buckling of shells having optimal positive Gaussian curvature. *Comput. Struct.* **1987**, *26*, 513–519. [CrossRef]
8. Błachut, J.; Smith, P. Tabu Search Optimization of Externally Pressurized Barrels and Domes. *Eng. Optim.* **2007**, *39*, 899–918. [CrossRef]
9. Błachut, J. Optimal Barreling of Steel Shells via Simulated Annealing Algorithm. *Comput. Struct.* **2003**, *81*, 1941–1956. [CrossRef]
10. Jam, J.E.; Kiani, Y. Buckling of Pressurized Functionally Graded Carbon Nanotube Reinforced Conical Shells. *Compos. Struct.* **2015**, *125*, 586–595. [CrossRef]
11. Babaei, M.; Kiarasi, F.; Hossaeini Marashi, S.M.; Ebadati, M.; Masoumi, F.; Asemi, K. Stress Wave Propagation and Natural Frequency Analysis of Functionally Graded Graphene Platelet-Reinforced Porous Joined Conical–Cylindrical–Conical Shell. *Waves Random Complex Media* **2021**, 1–33. [CrossRef]
12. Mollaei, S.; Babaei, M.; Asemi, K. Torsional Buckling of Functionally Graded Graphene Reinforced Composite Laminated Cylindrical Panel. *Arch. Appl. Mech.* **2023**, *93*, 427–435. [CrossRef]
13. Jasion, P.; Magnucki, K. Elastic Buckling of Barrelled Shell under External Pressure. *Thin-Walled Struct.* **2007**, *45*, 393–399. [CrossRef]
14. Magnucki, K.; Jasion, P. Analytical Description of Pre-Buckling and Buckling States of Barrelled Shells under Radial Pressure. *Ocean Eng.* **2013**, *58*, 217–223. [CrossRef]
15. Jasion, P.; Magnucki, K. Elastic Buckling of Horizontal Barrelled Shells Filled with Liquid—Numerical Analysis. *Thin-Walled Struct.* **2012**, *52*, 117–125. [CrossRef]
16. Zhang, J.; Peng, W.; Tang, W.; Wang, M. Experimental Study on the Geometrical and Mechanical Properties of Goose Eggshells. *Rev. Bras. Cienc. Avic.* **2017**, *19*, 455–464. [CrossRef]
17. Zhang, J.; Wang, M.; Wang, W.; Tang, W.; Zhu, Y. Investigation on Egg-Shaped Pressure Hulls. *Mar. Struct.* **2017**, *52*, 50–66. [CrossRef]
18. Zhang, J.; Wang, M.; Wang, W.; Tang, W. Buckling of Egg-Shaped Shells Subjected to External Pressure. *Thin-Walled Struct.* **2017**, *113*, 122–128. [CrossRef]
19. Zhang, J.; Zhu, B.; Wang, F.; Tang, W.; Wang, W.; Zhang, M. Buckling of Prolate Egg-Shaped Domes under Hydrostatic External Pressure. *Thin-Walled Struct.* **2017**, *119*, 296–303. [CrossRef]
20. Zhang, J.; Wang, M.; Cui, W.; Wang, F.; Hua, Z.; Tang, W. Effect of Thickness on the Buckling Strength of Egg-Shaped Pressure Hulls. *Ships Offshore Struct.* **2018**, *13*, 375–384. [CrossRef]
21. Liu, J.; Yu, B.; Zhou, Y.; Zhang, Y.; Duan, M. The Buckling of Spherical-Cylindrical Composite Shells by External Pressure. *Compos. Struct.* **2021**, 265. [CrossRef]
22. Zhang, M.; Tang, W.; Wang, F.; Zhang, J.; Cui, W.; Chen, Y. Buckling of Bi-Segment Spherical Shells under Hydrostatic External Pressure. *Thin-Walled Struct.* **2017**, *120*, 1–8. [CrossRef]
23. Zhang, J.; Di, C.; Wang, F.; Tang, W. Buckling of Segmented Toroids under External Pressure. *Ocean Eng.* **2021**, *239*, 109921. [CrossRef]
24. Di, C.; Zhang, J.; Wang, W.; Tang, W. Experimental and Numerical Study on the Buckling Performances of Segmented Toroidal Pressure Hulls. *China Mech. Eng.* **2021**, *32*, 2989–2994.
25. Yuan, S.; Fan, X. Developments and Perspectives on the Precision Forming Processes for Ultra-Large Size Integrated Components. *Int. J. Extrem. Manuf.* **2019**, *1*, 022002. [CrossRef]
26. Zhang, R.; Zhang, W.W.; Yuan, S.J. Research on Hydro-Forming of Spherical Shells with Different Preform Types. *Int. J. Adv. Manuf. Technol.* **2017**, *92*, 2631–2638. [CrossRef]
27. Zhang, W.W.; Yuan, S.J. Reverse Geometric Modeling for Pre-Form Shape of Prolate Ellipsoid before Hydro-Forming. *Int. J. Adv. Manuf. Technol.* **2017**, *88*, 1903–1909. [CrossRef]

28. Yuan, S.; Teng, B.; Wang, Z.R. A New Hydroforming Process for Large Elbow Pipes. *J. Mater. Process. Technol.* **2001**, *117*, 28–31. [CrossRef]
29. Zhang, J.; Wang, F.; Wang, F.; Tang, W.; Zhao, X. Free Bulging of Thin-Walled Cylinders Closed by Two Heavy Plates. *Ocean Eng.* **2021**, *223*, 108646. [CrossRef]
30. Zhang, J.; Wang, F.; Wang, F.; Zhao, X.; Tang, W.; Chen, F. Buckling Properties of Bulged Barrels under External Pressure. *Thin-Walled Struct.* **2021**, *168*, 108226. [CrossRef]
31. Zhang, J.; Dai, M.; Wang, F.; Tang, W.; Zhao, X.; Zhu, Y. Theoretical and Experimental Study of the Free Hydroforming of Egg-Shaped Shell. *Ships Offshore Struct.* **2022**, *17*, 257–267. [CrossRef]
32. Zhang, J.; Dai, M.; Wang, F.; Tang, W.; Zhao, X. Buckling Performance of Egg-Shaped Shells Fabricated through Free Hydroforming. *Int. J. Press. Vessel. Pip.* **2021**, *193*, 104435. [CrossRef]
33. Gou, P.; Cui, W.C. Study of Structural Optimization Problem for Multiple Intersecting Spherical Pressure Hulls. *Chuan Bo Li Xue/J. Ship Mech.* **2009**, *13*, 269–277.
34. Xiang, K. Numerical Analysis and Experimental Verification on Buckling of Multiple Intersecting Spherical Pressure Hull. Master's Thesis, Jiangsu University of Science and Technology, Zhenjiang, China, 2018.
35. Zhu, Y.; Dai, Y.; Ma, Q.; Tang, W. Buckling of Externally Pressurized Cylindrical Shell: A Comparison of Theoretical and Experimental Data. *Thin-Walled Struct.* **2018**, *129*, 309–316. [CrossRef]
36. *ENV 1993-1-6*; Eurocode 3—Design of Steel Structures—Part 1.6: Strength and Stability of Shell Structures. CEN: Brussels, Belgium, 2007.
37. China Classification Society (CCS). *Rules for the Classification and Construction of Diving Systems and Submersibles*; China Classification Society (CCS): Beijing, China, 2018.